RESEARCH ARTICLE

Decay of the drag wake of a sphere at Reynolds number 10^5

D. Curtis Saunders[1] · Justen A. Britt[1] · Scott Wunsch[1]

Abstract

The drag wake of a dimpled sphere with $Re = 10^5$ is studied experimentally using Stereo Particle Image Velocimetry to a downstream distance of ~ 90 diameters. The wake growth and velocity decay are analyzed and compared with previous dimpled sphere data for $Re = 5 \cdot 10^4$. Self-similar decay was observed with the ensemble mean axial velocity defect decaying as x^{-1} and the wake size growing as $x^{1/2}$. Due to the difference in Reynolds number, the two spheres have different drag coefficients (0.13 and 0.25, respectively), but these self-similar decay exponents were not observed to depend on drag coefficient or Reynolds number. The results suggest that the self-similar drag wake decay observed at laboratory scales may extrapolate to the larger Reynolds numbers typical of engineering and geophysical flows.

Graphical Abstract
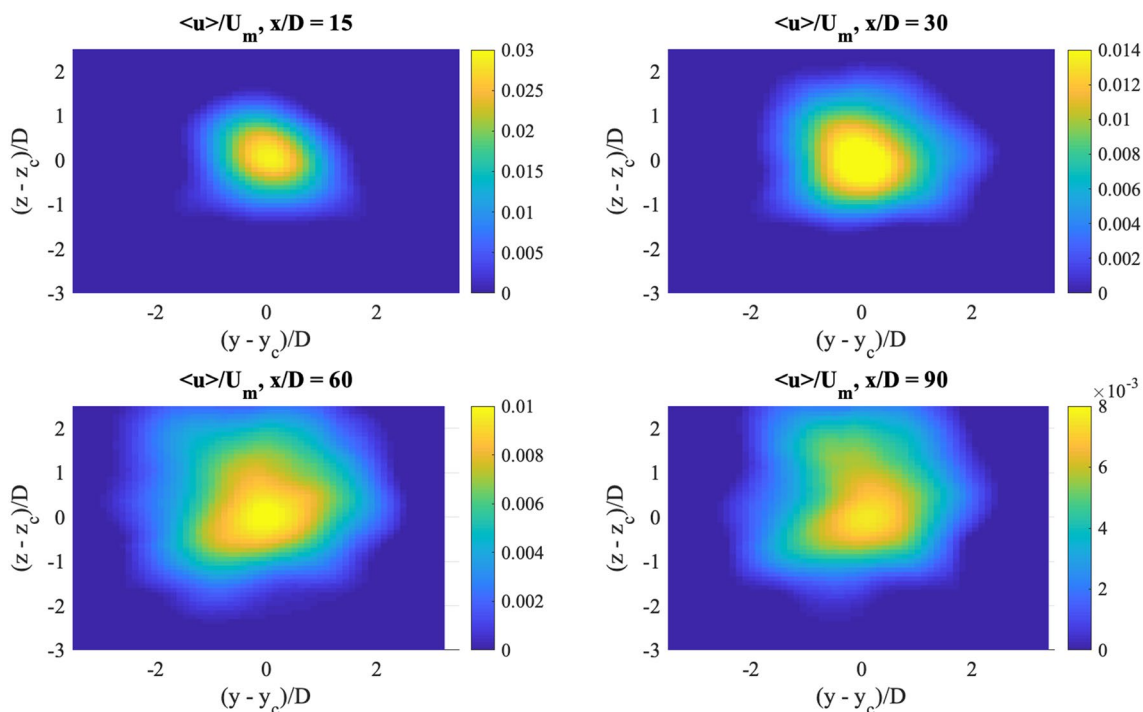
1 Introduction

The spreading and decay of the drag wake of an object is relevant to many applications in geophysics and engineering. Examples include the wakes of mountains, seamounts, windmills, and buildings. Drag wakes are characterized by

✉ D. Curtis Saunders
   Curtis.Saunders@jhuapl.edu

1   The Johns Hopkins University Applied Physics Laboratory,
    Laurel, MD, USA

their mean velocity defect as a function of distance x downstream from the generating body. For axisymmetric bodies such as spheres, disks, and slender cylindrical bodies, self-similar decay of the wake is typically observed (Tennekes and Lumley 1972). In this case, the mean velocity defect u (the difference between the flow speed U_m and the mean velocity component in the direction of travel x) has the functional form

$$\langle u(x, r) \rangle \simeq U_o(x) f\left(\frac{r}{L}\right) \tag{1}$$

$$L \sim \left(\frac{x}{D}\right)^{\alpha} \tag{2}$$

$$U_o \sim \left(\frac{x}{D}\right)^{-2\alpha} \tag{3}$$

where x/D is the downstream distance (measured in units of the body diameter D) and r is the radial distance from the center symmetry axis of the body. In this self-similar form, the radial profile of the wake velocity defect has the same shape $f(r/L)$ at any downstream distance when scaled by the appropriate velocity and length scales. The appropriate length scale L grows with some power α of x/D, while the velocity scale U_o decays twice as rapidly, as required by momentum conservation (Tennekes and Lumley 1972).

The classical self-similar scaling law (Swain 1929; Tennekes and Lumley 1972), in which the wake spreads with downstream distance x as $x^{1/3}$ ($\alpha = 1/3$ in Eqs. 1-3), has long been used to describe axisymmetric drag wakes. Although early experiments with spheres appeared to confirm this result (Bevilaqua and Lykoudis 1978), most recent experiments (Bonnier and Eiff 2002; Nedić et al. 2013; Obligado et al. 2016; Saunders et al. 2020) have demonstrated that axisymmetric drag wakes have more rapid wake spreading (as $x^{1/2}$, or $\alpha \simeq 1/2$ in Eqs. 1-3) and decay than the classical result of $\alpha = 1/3$. Experiments with a sphere at a Reynolds number ($U_m D/\nu$) of $Re \simeq 10^4$ first demonstrated non-classical decay to a distance of $\simeq 30$ body diameters. Non-classical scaling was extended to $\simeq 50$ body diameters

by Nedić et al. (2013). Although (Nedić et al. 2013) initially indicated that rough shapes (fractal plates) deviated from classical scaling while more smooth shapes (disks) did not, subsequent reanalysis in Obligado et al. (2016) found that all shapes studied had $\alpha \simeq 1/2$. However, other experiments with disks (Johanssan et al. 2003) have yielded classical scaling. Experiments with a dimpled sphere at $Re \simeq 5 \cdot 10^4$ (Saunders et al. 2020) also found $\alpha \simeq 1/2$ to a downstream distance of ~ 200 body diameters. High resolution numerical simulations have also reproduced the more rapid $x^{1/2}$ wake spreading (Dairay et al. 2015; Pal et al. 2017; Chongsiripinyo and Sarkar 2020; Nidhan et al. 2020), although (Nidhan et al. 2020) suggested a transition from $x^{1/2}$ to the slower $x^{1/3}$ growth at some downstream distance. While some questions remain, these results collectively appear to establish that non-classical ($\alpha \simeq 1/2$) wake decay occurs for most axisymmetric bodies at laboratory Reynolds numbers ($Re \sim 10^4$), at least over some initial distance downstream from the body.

Extrapolation of this laboratory scaling law to larger engineering applications with Reynolds numbers exceeding 10^5 remains an open question, as no data are available on wake decay at these Reynolds numbers. For spheres, the drag coefficient (and hence possibly the wake) undergoes a transition at Reynolds numbers of $\sim 10^5$, known as the 'drag crisis' (Achenbach 1972). As previous laboratory data were obtained at Reynolds numbers below this drag crisis, wake decay data in this transitional regime would provide insight into wake behavior at larger scales. To address this question, new Stereo Particle Image Velocimetry (SPIV) measurements of the decaying wake of a dimpled sphere with a Reynolds number of $Re = 10^5$ are compared to previous results for $Re = 5 \cdot 10^4$. Laboratory data from Achenbach (1974) indicate that the drag coefficient C_D for a rough sphere decreases from 0.5 to 0.1-0.2 (the 'drag crisis') for Reynolds numbers in the range of $\sim 5 \cdot 10^4$ to $\sim 3 \cdot 10^5$, with the transition point and minimum drag depending on surface roughness. As a consequence of the dimples on the sphere used here, the two Reynolds numbers compared fall within the drag crisis regime, and have different drag coefficients ($C_D \simeq 0.13$ for the new $Re = 10^5$ data,

Fig. 1 The dimpled sphere (left) and the experimental configuration (right)
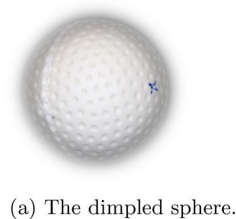
(a) The dimpled sphere.
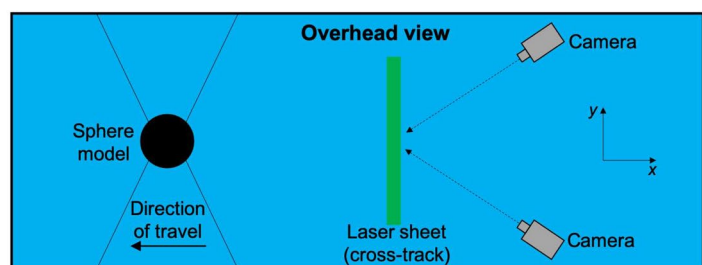
(b) A schematic of the experimental layout, illustrating the location of the towed sphere, SPIV cameras, and orientation of the laser illumination sheet.

compared to $C_D \simeq 0.25$ for $Re = 5 \cdot 10^4$ in Saunders et al. (2020)). These new data have been obtained near the drag minimum ($C_D \simeq 0.1$), and hence approach the flow regime found in engineering applications. The goal of the present experiments is to determine if this change in drag results in a measurable difference in the wake decay. This will assist in determining the applicability of the laboratory wake decay data to larger scale engineering flows.

2 Experimental approach

Experiments were conducted in the same tow tank as Saunders et al. (2020) using a dimpled sphere with a diameter of $D = 10$ cm towed at a constant speed of $U_m \simeq 1$ m/s. The sphere is a larger version of the one used in Saunders et al. (2020), and is shown in Fig. 1a. Figure 1b presents a schematic overhead view of the experiment. The tank width was 1.8 m and the water depth was 0.7 m. The blockage ratio (the square root of the ratio of sphere cross section to tank cross section) was $\simeq 0.08$, well below the threshold at which drag is impacted by the tank walls (Achenbach 1974). The sphere depth was approximately midway between the tank bottom and free surface. Surface disturbances were not observed during the experiments, indicating that interactions between the wake and free surface did not occur. A laser sheet originating beneath the tank floor and oriented perpendicular to the sphere direction of travel illuminated the particles within the wake. Two cameras in submerged boxes were located within the tank, one on each side of the wake at the same depth, to image the illuminated particles.

Stereo Particle Image Velocimetry (SPIV) data were acquired immediately following the passage of the sphere until wake structures reached the edge of the field of view of the SPIV system. The components of the SPIV system included the DaVis software (LaVision), two Imager sCMOS high speed cameras (LaVision), Camera Link HS Frame Grabber (LaVision), PTU-X Programmable Timing Unit (LaVision), and Litron Nano L 200-15 Pulsed Nd:YAG Laser. In addition, each camera was equipped with a Scheimpflug mount to correct for distortion due to the cameras not being perpendicular to the image plane. For these experiments the cameras were set to an angle of 33° from the x-axis (see Fig. 1b) and were fitted with 20 mm focal length lenses, resulting in an overlapping FOV of 73 cm in the y direction and 64 cm in the z direction. This angle is within the optimum range for SPIV systems, as determined by Lawson and Wu (1997).

The tank was seeded with 50 μm neutrally buoyant particles with an average density of 1.03 g/cc. The Stokes drift time scale of the particles was $\tau_p = 68$ μs (Raffel et al. 2018). For these experiments the timescale of the flow τ_f is given by the ratio of the length scale to the largest velocities in the wake. Therefore the Stokes number $S_t = \frac{\tau_p}{\tau_f}$, which is the ratio of these two scales, was approximately $3 \cdot 10^{-7}$ between $x/D = 15$ and $x/D = 90$. This Stokes number satisfies the requirement ($S_t \leq 10^{-1}$) for the seeding particles to follow the turbulent motions of the flow within the range of downstream distances studied. The 50 μm particle size was smaller than the resolution of the PIV system, indicating that pixel locking effects would be present in the data. However, this pixel size was chosen to obtain the field of view necessary to image the entire wake cross section at $x/D \sim 90$. Pixel-locking effects were reduced by both defocusing the cameras and by the subpixel interpolation scheme (Michaelis et al. 2016). Any remaining bias errors were further reduced by azimuthally averaging the resulting velocity fields before quantifying the mean and fluctuating velocity fields. The tank was seeded such that each interrogation region contained on average 8–10 particles. A dual-head Nd–Yag laser (Litron, 200 mJ/pulse, 532 nm wavelength) was used to illuminate the particles. This system contains two pulsed lasers which were aligned such that their optical paths were nearly identical. The laser sheet thickness was approximately 3 cm, ensuring the out-of-plane displacement was less than one-quarter of the light sheet thickness. The

Table 1 SPIV parameters

Re	Laser pulse rate (Hz)	Image pair time spacing δt (ms)	Min in plane velocity (cm/s)	Max in plane velocity (cm/s)	Uncertainty (cm/s)	No. of runs
$1 \cdot 10^5$ (Present data)	15	10	1	16	0.6	65
$5 \cdot 10^4$ (Saunders et al. 2020)	10	10	0.8	13	0.2	42

$Re = 1 \cdot 10^5$ corresponds to present study. Previous paremeters used in Saunders et al. (2020) are included as well corresponding to $Re = 5 \cdot 10^4$
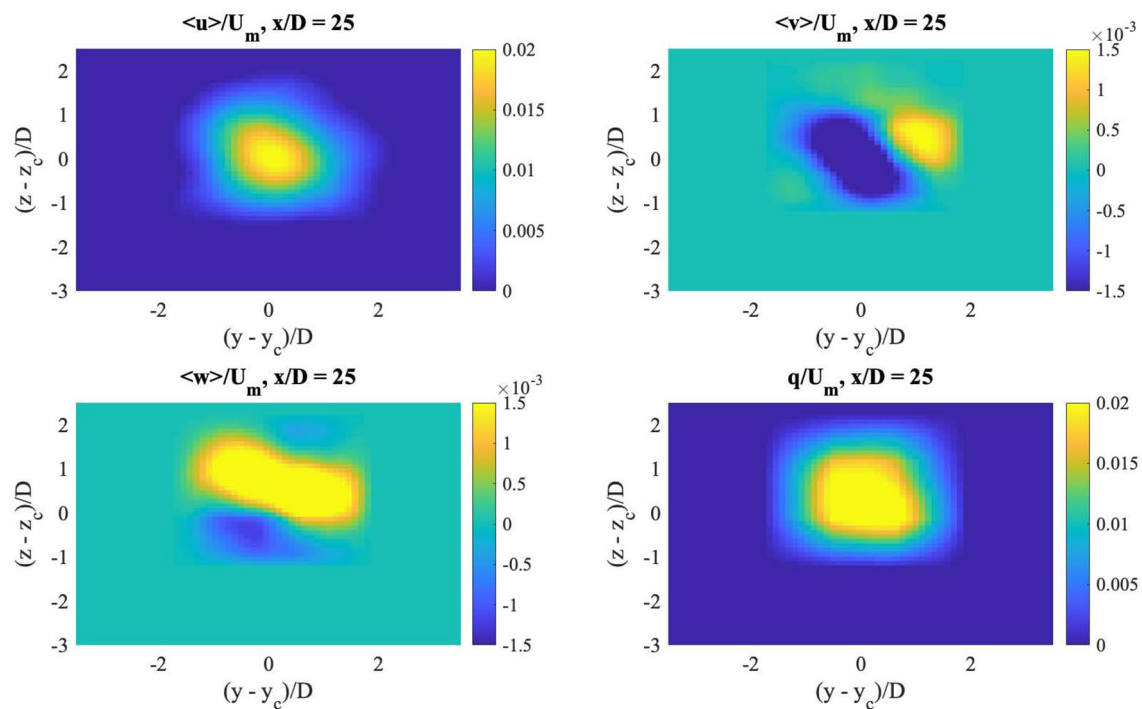
Fig. 2 Wake ensemble mean velocity components (u, v, and w) and fluctuations q at $x/D = 25$

lasers can be pulsed simultaneously or with a time delay between pulses. This time delay δt, combined with the desired spatial resolution and camera FOV, determines the range of flow velocity scales which can be measured.

Table 1 details the parameters used for the SPIV measurements. The SPIV processing was performed using an open-source MATLAB code called UVMAT (xxxx). The algorithm first performs PIV processing of the images from a single camera using a dual-pass method, where the first pass determines lower-resolution estimates of the velocity field within an interrogation region, while the second pass uses the estimates from the first pass to obtain more precise measurements of the velocity field at a higher resolution. The velocity fields from the two cameras are then combined using SPIV to determine all three velocity components within the plane of data. The first-pass PIV analysis was performed with 128×128 pixel interrogation regions, a search-box size of 147×147 pixels, a shift of $(0,0)$ pixels, and a 50 % overlap of the interrogation regions. The second-pass analysis was performed with interrogation regions of 64×64 pixels and a 50 % overlap, resulting in a velocity vector every 32 pixels in the y and z directions. These window sizes ensured that particle displacements were limited to 1/4 of the interrogation window, corresponding to a maximum in-plane velocity of 26 cm/s. Subpixel accuracy was obtained using the thin plate spline method. This is a multi-dimensional generalization of spline interpolation and is an optimum way

to interpolate data with minimal curvature of the interpolating function (UVMAT xxxx).

While the Stokes numbers indicated the particles would accurately follow turbulent motions within the fluid, the errors in detecting particle positions and ultimately fluid velocities were also quantified. Given the size of the particles (≤ 1 pixel), we estimate a measurement uncertainty on the order of 0.3 pixels (Raffel et al. 2018). This corresponds to a velocity error of up to 0.6 cm/s. Typical particle displacements were from 3 to 6 pixels, corresponding to wake in-plane velocities from 7 to 11 cm/s. Additionally, the typical shear across the interrogation window was less than 0.02 pixels. Displacement estimates with correlations above 50% were kept and the remaining values were discarded.

Sixty-five runs were performed so that the results could be combined to produce estimates of the ensemble mean and fluctuating velocity fields. The SPIV settings for the present $Re = 10^5$ experiments were sufficient to collect accurate velocity data in the downstream range of $15 \leq x/D \leq 90$. The prior experiments of Saunders et al. (2020) also yielded acceptable velocity data in this range, allowing direct comparison of the two Reynolds numbers. To obtain the mean axial velocity, the measured axial velocity fields from each experiment at a given x/D were averaged. The velocity fluctuation field is defined as the standard deviation of the velocity components over the ensemble of experiments at each x/D. The tow speed varied by less than 1 cm/s between runs so all SPIV velocities were normalized by the nominal tow
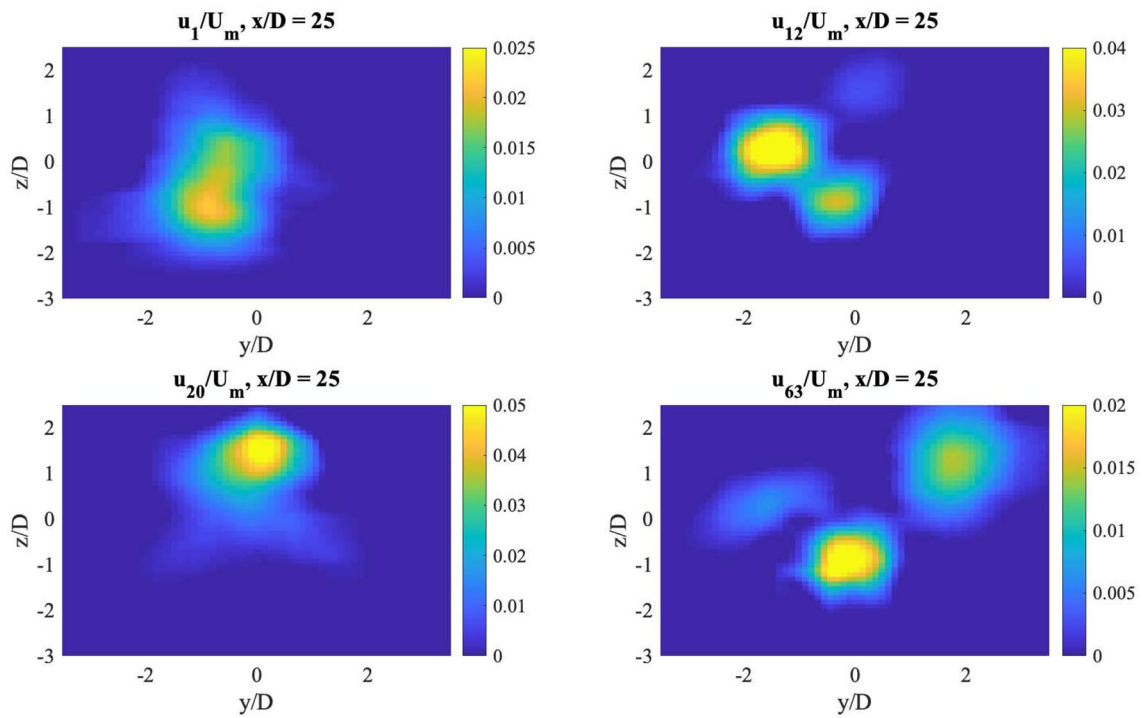
Fig. 3 Individual realizations of the axial velocity defect u at $x/D = 25$
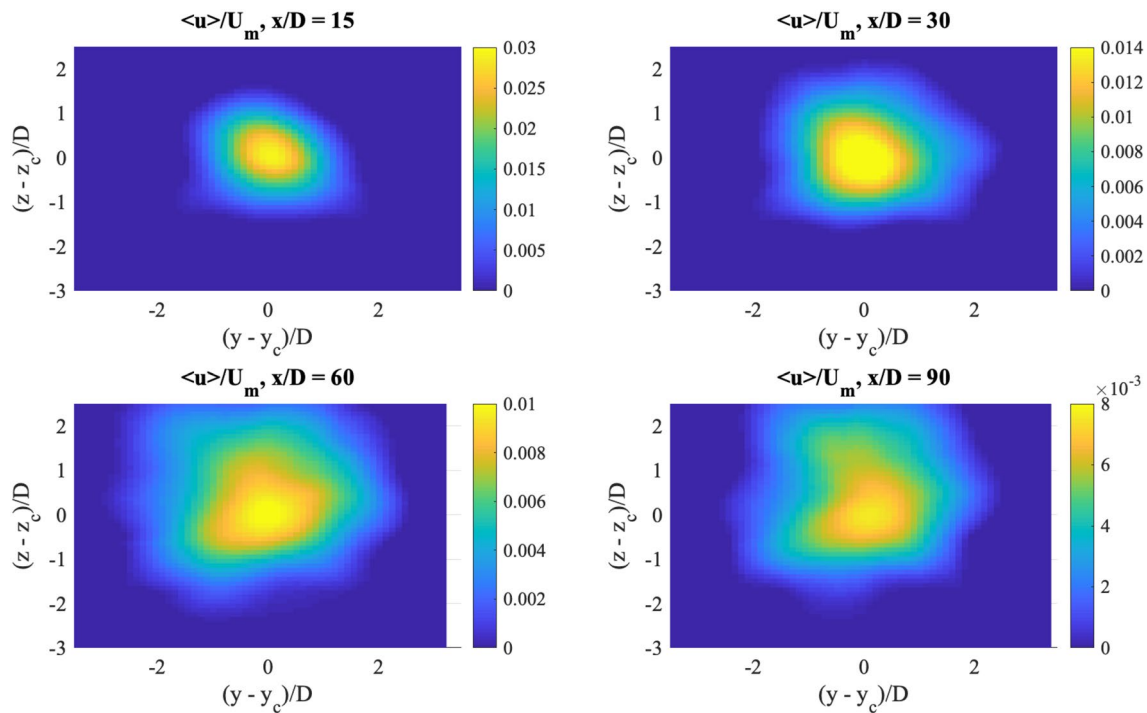

Fig. 4 Ensemble mean axial velocity defect $\langle u \rangle / U_m$ at 4 down-track locations
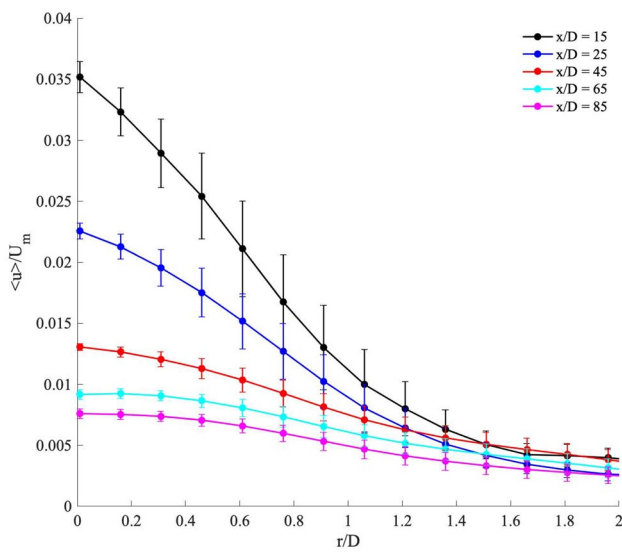
Fig. 5 Ensemble mean axial velocity defect U_m as a function of radius r/D at 5 down-track locations

Fig. 6 Self-similar profiles of the mean axial velocity defect U_o as a function of radius r/L_u at the same locations as Fig. 5, using the similarity scales computed from Eqs. 7 and 8

speed of 1 m/s. There is also a variation in the depth and horizontal position of the wake center from run to run, due to slightly nonzero drift velocities which vary from run to run. This effect was mitigated by averaging the runs.

3 Results

Figure 2 presents the SPIV ensemble mean velocity field (averaged over 65 runs) measured at $x/D = 25$. The upper left panel shows the mean axial velocity defect u normalized by the sphere tow speed U_m. The wake appears as the yellow region in the center of the panel. This view demonstrates the approximately axisymmetric shape of the mean axial velocity defect. The upper right and lower left panels present the mean horizontal and vertical velocities, respectively. These components are an order of magnitude smaller than the mean axial velocity defect. Note that the ensemble mean velocities for the v and w components (~ 3 mm/s) at $x/D = 25$ are smaller than the SPIV accuracy for an individual run. Averaging the 65 runs reduces the effective error of the ensemble mean by a factor of $1/\sqrt{65} \sim 1/8$, for an error of ~ 0.8 mm/s in the ensemble mean.

The lower right panel of Fig. 2 presents the root-mean-square fluctuation velocity q for the ensemble of runs. Here q is defined as

$$q^2 \equiv \frac{1}{2}\langle (u - \langle u \rangle)^2 + (v - \langle v \rangle)^2 + (w - \langle w \rangle)^2 \rangle \tag{4}$$

At this x/D, the magnitude of these fluctuations is comparable to the mean axial velocity. The axial velocity defects of four individual runs at $x/D = 25$ are illustrated in Fig. 3.
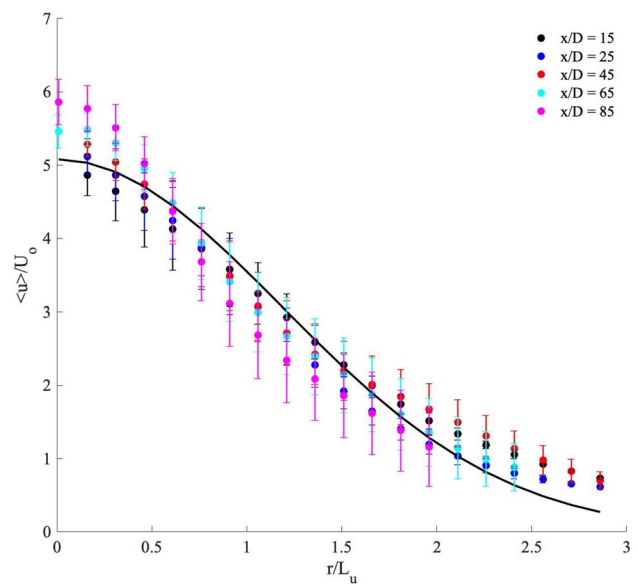
There are large variations in axial velocity defect from run to run, and individual runs do not appear axisymmetric. As a result, no individual wake realization closely resembled the mean flow field. The variations from run to run are responsible for the magnitude of q seen in the lower right panel of Fig. 2. These variations also necessitate the large number of experimental runs (65) conducted to obtain quality ensemble-mean data.

The decay of the mean axial velocity defect is illustrated in Fig. 4, which presents the wake defect at four x/D locations from 15 to 90. The wake grows in size and its peak velocity decays with distance, as expected (note changing color scales). Observed deviations from axisymmetry tend to increase with downtrack distance, but remain modest even at $x/D = 90$. This asymmetry is attributed to a relative increase in wake fluctuations at greater x/D, requiring more runs to be averaged to obtain a quality estimate of the mean.

To explore self-similar decay, the wake size and mean axial velocity defect scales are characterized as a function of x/D using the same approach as Saunders et al. (2020). The SPIV ensemble mean axial velocity data in a small range of x/D are binned into radial segments (based on distance from the sphere center) and averaged over azimuth to produce profiles of $\langle u(x, r) \rangle$. This azimuthal averaging procedure exploits the expected axisymmetry of the wake. Here, radial bins of $0.1D$ and x/D bins of $\pm 0.1x/D$ were used. Radial profiles of $\langle u \rangle$ at 5 locations are presented in Fig. 5, demonstrating the spreading of the wake mean axial velocity defect as x/D increases.
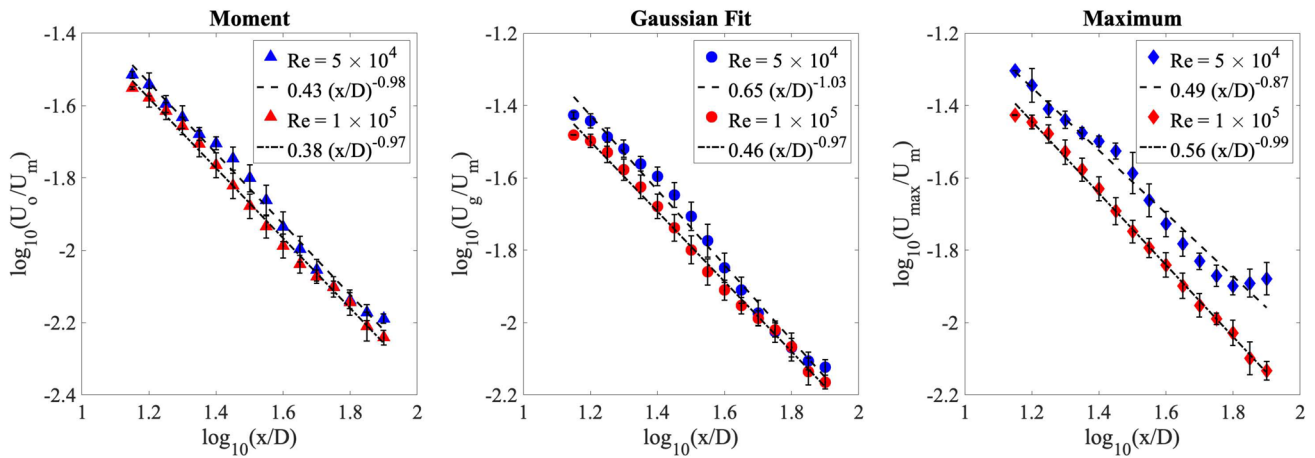
Fig. 7 Mean axial velocity decay (colored symbols) as a function of x/D, along with best-fit scaling exponents (black lines). Present $Re = 10^5$ data are shown in red; $Re = 5 \cdot 10^4$ data from Saunders et al. (2020) are shown in blue. Each panel presents a different method for estimating the velocity scale: *Left:* Moments (Eqs. 5 and 6) *Center:* Gaussian fit *Right:* Maximum of the ensemble mean axial velocity defect

From the profiles in Fig. 5, the first two moments are computed at each x/D:

$$M_o(x) \equiv \int_0^\infty \langle u(x, r) \rangle r \, dr \qquad (5)$$

$$M_2(x) \equiv \int_0^\infty \langle u(x, r) \rangle r^3 \, dr \qquad (6)$$

In practice, the integration range is limited to $r < 2.5D$, to avoid contamination by measurement noise far from the wake center. Using these moments, the wake size L_u and mean axial velocity scale U_o are computed from

$$L_u^2 \equiv \frac{M_2}{M_o} \qquad (7)$$

$$U_o \equiv \frac{M_o^2}{M_2} \qquad (8)$$

These represent the typical length and velocity scales of the wake, based on the measured profiles in Fig. 5. This approach makes no assumption regarding the shape of the mean axial velocity defect profile. Figure 6 presents the mean axial velocity defect profiles from Fig. 5 normalized by the length scale $L_u(x)$ and velocity scale $U_o(x)$ computed using Eqs. 7 and 8. The results demonstrate that the mean axial velocity defect profile is approximately self-similar

Fig. 8 Wake growth as a function of x/D, along with best-fit growth exponents
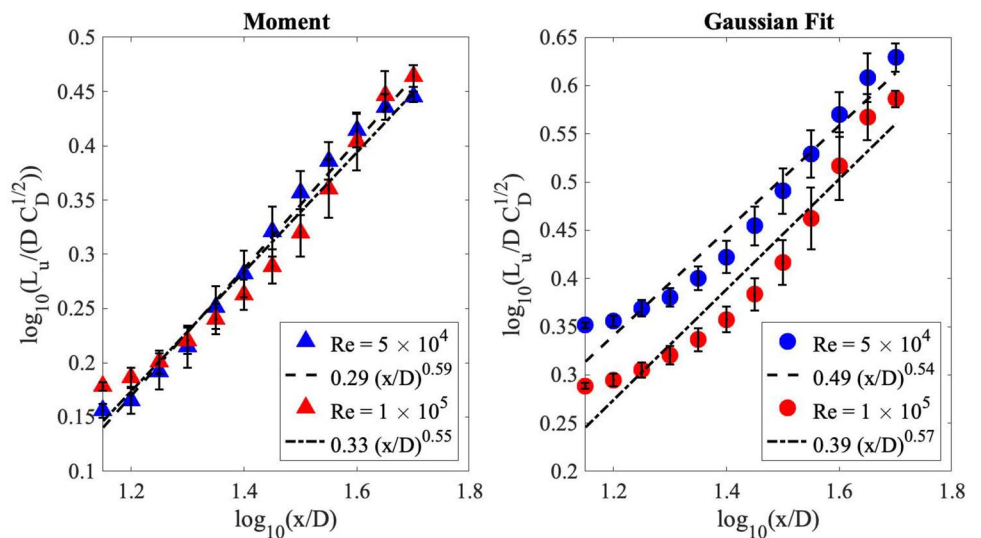
when normalized by these scales. Also shown in Fig. 6 is a Gaussian fit to the profile (black line), which is found to be a reasonable approximation to the profile shape to $r \simeq 2L_u$.

The decay of the mean axial velocity defect scale U_o with x/D is presented in Fig. 7. The data were binned in distance x/D using a logarithmic scale with a bin width of $\log_{10}(x/D) = 0.05$. Logarithmic scales are used in Fig. 7 so the power law decay (Eq. 3) yields a straight line. Data from the present $Re = 10^5$ experiments are shown in red. The panels present three independent measures of the velocity scale, all of which are expected to decay with the same exponent due to self-similarity. The left panel presents the result of Eq. 8, as in Saunders et al. (2020). This is the velocity scale that produced the self-similar collapse in Fig. 6. The center panel presents the velocity magnitude for a Gaussian fit to the profile at each x/D (as in Fig. 5), and the right panel shows the maximum of the ensemble-mean velocity defect at each x/D, as in Bonnier and Eiff (2002). The error bars in Fig. 7 represent one standard deviation of values within each logarithmic bin. The best-fit power law for each measure of the velocity scale is shown as a black dash-dot line. All three measures yield a best-fit decay exponent -2α (Eq. 3) of approximately -1. Also shown in blue in each panel are the $Re = 5 \cdot 10^4$ data from the previous dimpled sphere experiments of Saunders et al. (2020) for the same range of x/D. The wake ensemble mean axial velocity defect data for the two different values of Re closely align, with similar decay exponents of ~ -1 for both the moments (left panel) and Gaussian fit (center panel) methods. The maximum of the mean velocity defect (right panel) for the previous $Re = 5 \cdot 10^4$ data (blue) yielded a slower decay (exponent ~ -0.9) but also exhibited greater scatter. However, the full
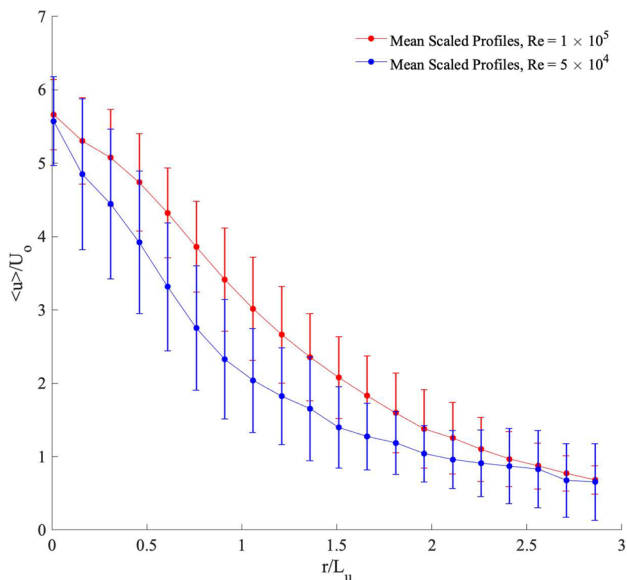

Fig. 9 Self-similar profiles of the mean axial velocity defect $< EmphasisType = \varepsilon Underline\varepsilon > /U_o$ as a function of radius r/L_u

data set in Saunders et al. (2020) for maximum mean velocity defect (covering a greater range of x/D) yielded a best-fit exponent of $\simeq -1$, consistent with the other methods. The agreement between the two Reynolds numbers suggests that the observed wake mean axial velocity decay exponent of -1 may not change as Re increases from laboratory to engineering scales.

Spheres with different drag coefficients generate wakes with different total momentum fluxes, and this must be reflected in the mean wake velocity defect and/or length scales. The total momentum flux defect in the wake (found by integrating the mean velocity defect at any x/D and multiplying by U_m) is proportional to $U_m^2 M_o$, and the drag coefficient can be estimated from the integrated mean axial velocity defect using

$$C_D = \frac{16 M_o}{U_m D^2} = 16 \left(\frac{U_o}{U_m} \right) \left(\frac{L_u}{D} \right)^2 \tag{9}$$

The drag coefficient has been estimated here from the mean axial velocity data for $15 \leq x/D \leq 30$. For the present data with $Re = 10^5$, the result is $C_D = 0.13 \pm 0.01$, while the corresponding result for the $Re = 5 \cdot 10^4$ dimpled sphere data of Saunders et al. (2020) is $C_D = 0.25 \pm 0.01$. This reduction in drag coefficient with Reynolds number is consistent with the 'drag crisis' for a rough sphere seen in the laboratory data of Achenbach (1974). The difference in drag coefficients between the two Reynolds numbers requires that the product $U_o L_u^2$ for the two cases differ. The new $Re = 10^5$ data in Fig. 7 have a velocity scale U_o/U_m that is 10–15 percent less than the previous $Re = 5 \cdot 10^4$ values for a given x/D. Because of this small difference between the two values of U_o/U_m, it is expected that the length scale L_u/D must be larger for the larger C_D case, due to the greater total momentum of the wake.

Figure 8 presents the length scale L_u (Eq. 2) of the wake mean axial velocity defect as a function of x/D as computed from the mean axial velocity defect profiles in Fig. 5. The left panel presents the result from the moments (Eq. 7) of the profiles yielding the self-similar collapse in Fig. 6, while the right panel presents the result of a Gaussian fit to the profiles in Fig. 5. Present results for $Re = 10^5$ are again shown in red, while prior results for $Re = 5 \cdot 10^4$ are in blue (Saunders et al. 2020). The vertical axis is shifted by $\log_{10}\sqrt{C_D}$ to approximately compensate for the difference in drag between the two cases, as suggested by Eq. 9 with U_o/U_m being approximately independent of C_D. The error bars represent one standard deviation of values within each logarithmic bin. The wake growth exponent is $\alpha \simeq 1/2$, as expected for consistency with the velocity decay exponent of $-2\alpha \simeq -1$ in Fig. 7. The two Reynolds numbers have the same growth exponent, but the wake is smaller for the larger Re, lower
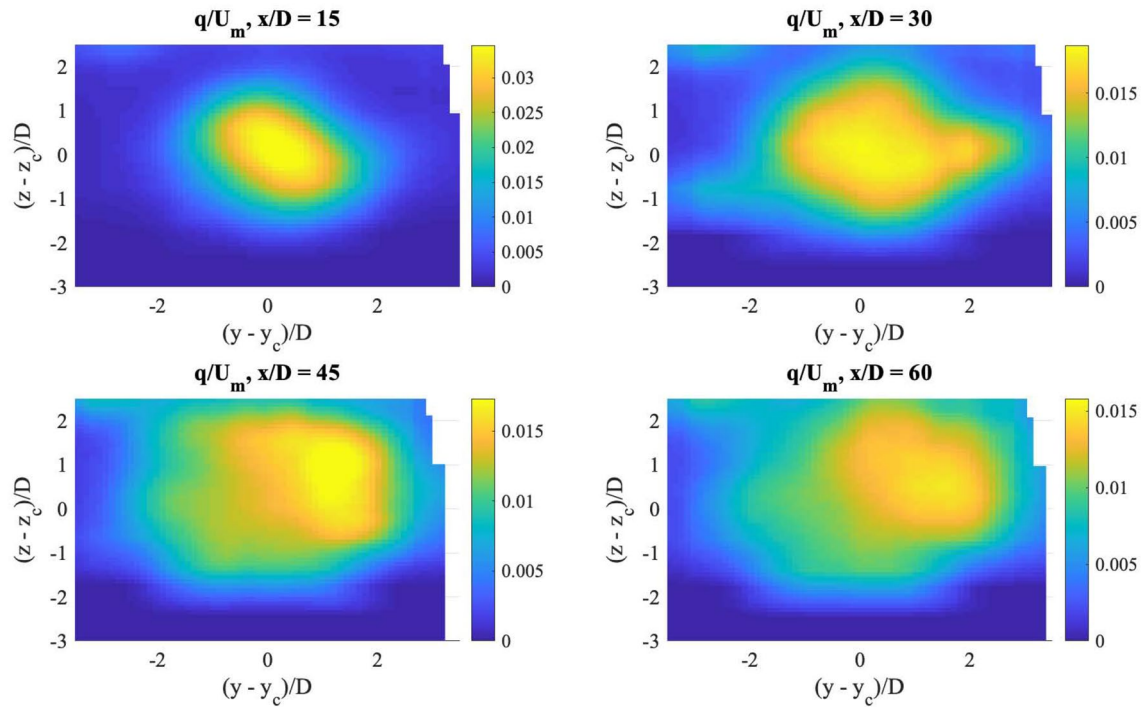
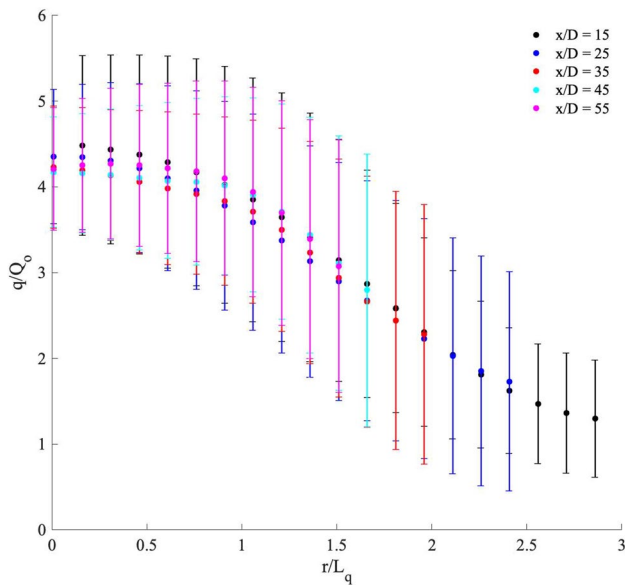**Fig. 10** Velocity fluctuations q/U_m at 4 down-track locations

Fig. 11 Self-similar profiles of the velocity fluctuation q/Q_o as a function of radius r/L_q at 5 down-track locations

drag case, with the reduction factor given approximately by the square root of the drag coefficient ratio.

Some previous studies (Johanssan et al. 2003; Nedić et al. 2013; Obligado et al. 2016) have utilized a virtual origin in x/D for the estimation of the wake growth and velocity decay exponents, while others (Bonnier and Eiff 2002; Saunders

et al. 2020) have not. The method of Obligado et al. (2016) has been applied to both data sets for U_o and L_u (not shown). In all cases, virtual origins were found to be less than $1.5D$ in magnitude, and the best-fit exponents within 0.05 of the values shown here. The modest impact of the virtual origin is attributed to the starting point being downstream (larger x/D) from the starting point of previous studies (Johanssan et al. 2003; Nedić et al. 2013; Obligado et al. 2016).

Figure 9 compares the mean axial velocity defect shape functions $f(r/L_u)$ from Eq. 1 for the two Reynolds numbers. Here the velocity and radial distance are scaled by U_o and L_u, respectively. The shape function shown in red is an average of the shape functions at different x/D from Fig. 6 for $Re = 10^5$. Blue presents the corresponding average shape function from Saunders et al. (2020). The larger Reynolds number case appears to have a modestly larger shape function for r/L_u between ~ 0.5 and ~ 2, but the error bars overlap so this observation is not conclusive.

Other wake characteristics, such as velocity fluctuations and Reynolds stress, are also expected to demonstrate self-similar decay. The fluctuation q (Eq. 4 and Fig. 2, lower right panel) from the ensemble-mean wake velocity defect should follow a self-similar decay:
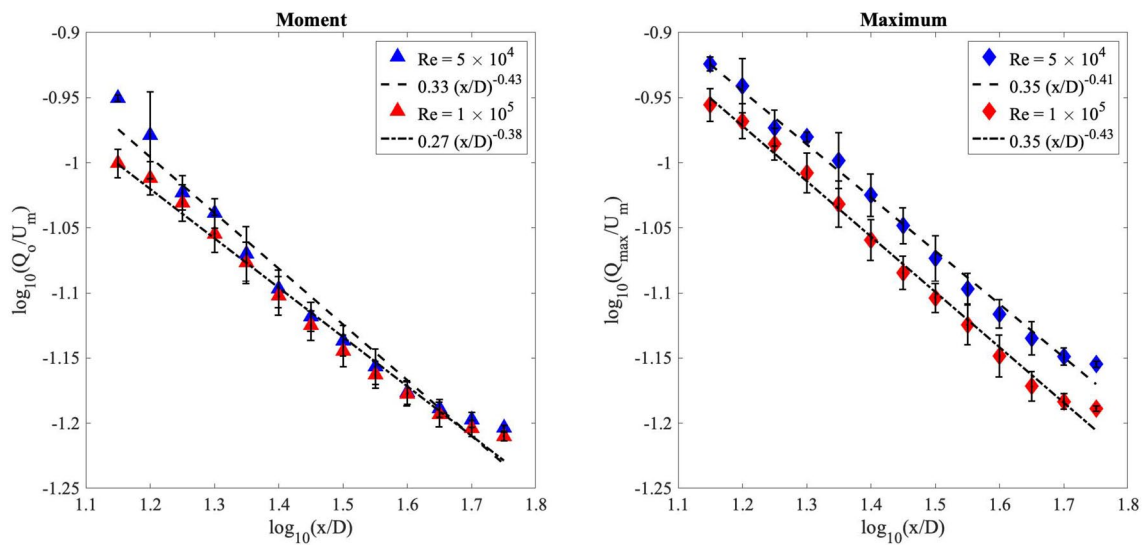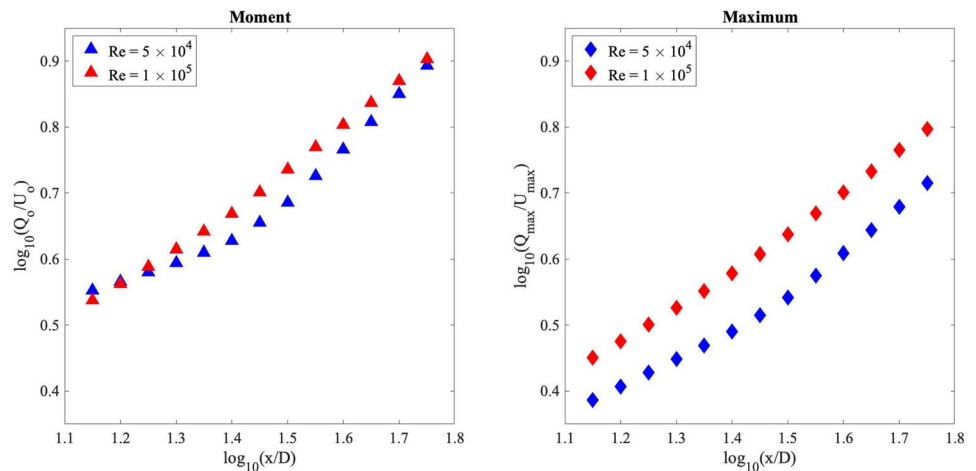
$$q(x,r) \simeq Q_o(x)g\left(\frac{r}{L_q}\right) \qquad (10)$$

Fig. 12 Velocity fluctuation (Q_o) decay (colored symbols) as a function of x/D, along with best-fit decay exponents (black lines)

Fig. 13 Growth of Q_o/U_o as a function of x/D for the two Re values tested

where Q_o scales with some power of x/D. The spreading and decay of the velocity fluctuations q at four x/D locations are presented in Fig. 10. Like the mean axial velocity defect (Fig. 4), the q field spreads and decays with downtrack distance (note changing color scales). Quality statistics for this quantity require more runs than are needed for the mean axial velocity defect, and the number of runs required increases with x/D. The present data yield approximately axisymmetric results for q to $x/D \sim 60$, and as can be seen in the lower panels of Fig. 10, symmetry is imperfect for the larger values of x/D shown. Self-similar decay of velocity fluctuations q is studied here only within this more limited range of x/D.

The characteristic scales of the velocity fluctuations q are computed as in Saunders et al. (2020) by replacing $\langle u \rangle$ with q in the moment equations (Eqs. 5 and 6) to yield a second length scale L_q^2 and velocity scale Q_o. Figure 11 presents the

self-similar fluctuation profiles $q(r/L_q)/Q_o$ for five values of x/D. Error bars, indicating the standard deviation in q within each data bin, are larger than in Fig. 6 due to the larger variability in this quantity than in the mean axial velocity defect. Although consistent with self-similarity, the larger error bars make it difficult to discern with confidence how well the profiles at different x/D collapse.

The decay of the fluctuation velocity scale Q_o is presented in the left panel of Fig. 12. In addition, the maximum fluctuation velocity in each x/D bin is included as Q_{max} in the right panel. For the present data (shown in red), the fluctuation velocity scale Q_o decays more slowly with x/D than U_o, with a decay exponent of ~ -0.4. Again, two differing approaches (the moment calculation and the maximum of q) are used to confirm the scaling, but the Gaussian fit is not used here as the shape profile is not Gaussian (see Fig. 11). Also shown in blue in Fig. 12 are previous results for $Re = 5 \cdot 10^4$ from

Saunders et al. (2020). The best-fit exponents for the two Reynolds numbers are both $\simeq -0.4$, and the difference in the magnitude of the velocity fluctuations between the two experiments is less than ten percent at each x/D.

A key observation regarding the fluctuation scale Q_o is that it decays much more slowly with x/D than the mean axial velocity defect scale U_o. This is illustrated in Fig. 13, which presents the ratio of the two velocity scales. As x/D increases, the wake is increasingly dominated by fluctuations. By $x/D \sim 60$, the fluctuations are nearly an order of magnitude larger than the mean axial velocity defect. This is true for both Reynolds numbers tested.
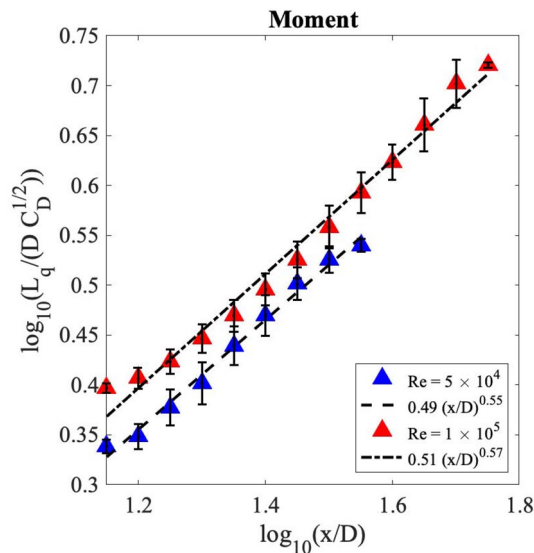

Fig. 14 Wake growth as a function of x/D based on velocity fluctuations, along with best-fit growth exponents
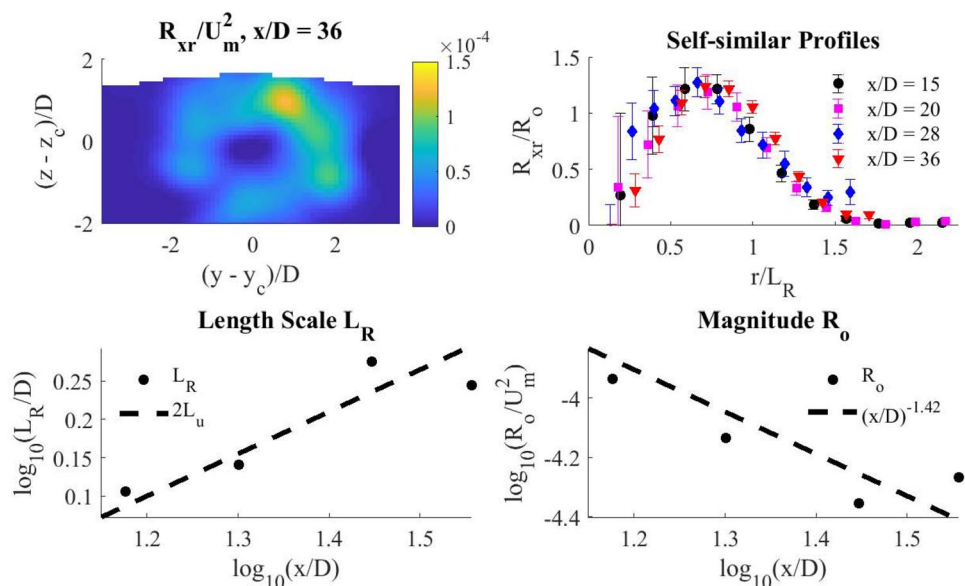
Figure 14 presents the length scale L_q, along with its best-fit scaling exponent. The vertical axis shows $L_q/\sqrt{C_D}$ for consistency with the presentation of L_u in Fig. 8. For self-similar wake decay it is expected that the length scales L_u and L_q for mean and fluctuating velocity are proportional. The velocity fluctuation scale L_q increases with x/D with an exponent of 0.57 ± 0.04, while L_u (Fig. 8) has a similar value of 0.55 ± 0.03. Self-similarity requires that these two exponents are equal, as there should be only one length scale (up to a constant of proportionality), and the data are consistent with this expectation. The fluctuation length scale L_q is typically about 60 percent larger than L_u, but the growth exponents are comparable. Figure 14 also shows the comparable result for $Re = 5 \cdot 10^4$ in blue. These data have a similar growth exponent but a length scale (normalized by diameter) that is nearly twice as large as the $Re = 10^5$ case. The smaller range of x/D shown for the $Re = 5 \cdot 10^4$ case reflects the limitation of the smaller SPIV field of view in the earlier experiments.

The Reynolds stress is another wake characteristic expected to demonstrate self-similar decay. Data were analyzed for the radial component of the Reynolds stress R_{xr}, defined as

$$R_{xr} \equiv \langle uv_r \rangle - \langle u \rangle \langle v_r \rangle \tag{11}$$

where v_r is the radial velocity and $\langle ... \rangle$ again denotes an average over the ensemble of experimental runs. For self-similar wake decay, this component of Reynolds stress can be expressed in terms of a magnitude R_o and a length scale L_R as

Fig. 15 The radial component of the Reynolds stress. *Upper left:* Measured Reynolds stress at $x/D \sim 36$. *Upper right:* Self-similar profiles of Reynolds stress at four x/D. *Lower left:* The length scale L_R used to normalize the self-similar profiles, along with the length scale for the mean velocity defect L_u. *Lower right:* The magnitude R_o used to normalize the self-similar profiles, along with a line with exponent -1.42

Table 2 Exponent comparison

Quantity	Size (L_u)	Mean velocity (U_o)	Velocity fluctuations (q)
$Re = 10^5$ (present)	0.55 ± 0.07	-0.97 ± 0.04	-0.38 ± 0.03
$Re = 5 \cdot 10^4$ (Saunders et al. 2020)	0.57 ± 0.07	-0.98 ± 0.05	-0.43 ± 0.05

$$R_{xr}(x, r) \simeq R_o(x) h\left(\frac{r}{L_R}\right). \tag{12}$$

This is analogous to Eq. 1 for the mean velocity defect and Eq. 10 for the velocity fluctuations. This stress component has previously been shown to decay self-similarly to $x/D = 50$ in lower Reynolds number experimental (Nedić et al. 2013) and numerical (Obligado et al. 2016) studies of disks and fractal shapes, but the $Re = 5 \cdot 10^4$ sphere experiments of Saunders et al. (2020) did not include a sufficient number of runs to obtain quality statistics on this quantity.

Figure 15 presents data from the present $Re = 10^5$ experiments on the decay of the Reynolds stress component R_{xr}. The upper left panel presents R_{xr} at $x/D = 36$, averaged over a range of $\pm 0.1 x/D$. The azimuthal symmetry is apparent, although imperfect as more data would likely be needed for better statistical convergence. Deviations from azimuthal symmetry were observed to increase with x/D. The stress is zero at the center of the wake, and has a maximum value at a radius of $\simeq 1.5D$. The maximum value is $\simeq 10^{-4} U_m^2$, approximately a quarter of the velocity fluctuations q^2 at this x/D. The magnitude is smaller than q^2 because the radial velocity v_r is smaller than the axial velocity (see Fig. 2), which also makes R_{xr} a more challenging measurement than q^2.

The upper right panel of Fig. 15 presents azimuthally averaged self-similar profiles for $R_{xr}(r)$ at four x/D locations. As with the previously analyzed quantities, data are binned in x/D with a bin of $\pm 0.1 x/D$ to improve the statistics. The magnitude R_o and length scale L_R at each x/D were computed from the azimuthally averaged profiles using the moment method (Eqs. 5 and 6) analogous to the other quantities presented. The Reynolds stress from these locations approximately collapse, as expected. The shape is similar to that reported in Nedić et al. (2013); Obligado et al. (2016), with an off-center peak at $r \sim 0.8 L_R$. The length scales L_R and magnitudes R_o computed for the self-similar profiles are shown in the lower panels of Fig. 15. The length scale L_R (lower left) is expected to be proportional to L_u and L_q. The dashed line, corresponding to $2L_u$, shows that the computed values of L_R are consistent with self-similarity. According to self-similar theory (Nedić et al. 2013; Obligado et al. 2016; Saunders et al. 2020), the magnitude R_o should obey $R_o \sim U_o U_m d L_u / dx$. For the measured best-fit scaling exponents of U_o (-0.97) and L_u (0.55), this yields a scaling exponent of -1.42. The black dashed line in the lower right panel of Fig. 15 shows that the computed values

of R_o are consistent with this exponent. Best-fit values of the scaling exponents for L_R and R_o were not computed due to the relatively small range of x/D for which adequate statistics for R_{xr} were obtained. The data presented for R_{xr} are consistent with self-similar theory, but are not sufficient to show that the Reynolds stress obeys self-similar theory for the full range of data collected (to $x/D \simeq 90$).

4 Discussion

This is the first experimental study of self-similar drag wake decay at a Reynolds number (based on diameter) of $Re = 10^5$ extending to a downstream distance of $x/D = 90$. The mean axial velocity defect decayed with an exponent of $\simeq -1$ while the wake size grew with exponent $\simeq 0.5$. The results are consistent with prior data for a sphere at $Re = 5 \cdot 10^4$ (Saunders et al. 2020) as well as recent results from other axisymmetric shapes (Bonnier and Eiff 2002; Nedić et al. 2013; Obligado et al. 2016) at lower Re, but differ from the long-standing and previously accepted classical self-similar scaling exponents of $-2/3$ and $1/3$, respectively (Swain 1929; Tennekes and Lumley 1972). Table 2 summarizes the wake scaling exponents found in the present study compared to previous experiments at a lower Reynolds number. Scaling exponents for the wake size, mean axial velocity magnitude, and velocity fluctuation magnitude are all identical to within error estimates for both Re. The similarity in wake decay between the two Reynolds numbers occurred despite a difference in drag coefficients of nearly a factor of two, owing to the flow transition associated with the 'drag crisis' at these Reynolds numbers (Achenbach 1974). This consistency in observed wake decay exponents despite the change in flow regime suggests that these laboratory results may pertain to larger Reynolds number engineering flows. (Note that the exponents for $Re = 5 \cdot 10^4$ in Table 2 differ slightly from those reported in Saunders et al. (2020) because a larger range of x/D, obtained using multiple SPIV settings, was used. Here the fitting range of x/D was restricted to match the present $Re = 10^5$ data, so that the best-fit exponents would reflect the same x/D range.)

Another observation common to both Reynolds numbers is the increasing importance of fluctuations relative to the ensemble mean as x/D increases. The fluctuation velocity scale decreases with an exponent of $\simeq -0.4$, less than half of the decay rate of the mean axial velocity defect. The ratio

of fluctuations to the ensemble mean therefore grows with x/D. Individual realizations of the wake appear less and less like the ensemble mean as x/D increases.

Author Contributions Curtis Saunders contributed to the experimental setup, data collection, data processing and analysis. Justen Britt contributed to the experimental setup and data collection. Scott Wunsch contributed to the experimental design, data processing and analysis.

References

Achenbach E (1972) Experiments on the flow past spheres at very high Reynolds numbers. J Fluid Mech 54:565–575

Achenbach E (1974) The effects of surface roughness and tunnel blockage on the flow past spheres. J Fluid Mech 65:113–125

Bevilaqua PM, Lykoudis PS (1978) Turbulence preservation in self-preserving wakes. J Fluid Mech 89:589–606

Bonnier M, Eiff O (2002) Experimental investigation of the collapse of a turbulent wake in a stably stratified fluid. Phys Fluids 14:791–801

Chongsiripinyo K, Sarkar S (2020) Decay of turbulent wakes behind a disk in homogeneous and stratified fluids. J Fluid Mech 885:A31-1

Dairay T, Obligado M, Vassilicos JC (2015) Non-equilibrium scaling laws in axisymmetric turbulent wakes. J Fluid Mech 781:166–195

Johanssan PBV, George WK, Gourlay MJ (2003) Equilibrium similarity, effects of initial conditions and local Reynolds number on the axisymmetric wake. Phys Fluids 15(3):603–617

Lawson NJ, Wu J (1997) Three-dimensional particle image velocimetry: experimental error analysis of a digital angular stereoscopic system. Meas Sci Technol 8:1455–1464

Michaelis D, Neal D, Wieneke B (2016) Peak-locking reduction for particle image velocimetry. Meas Sci Technol 27:104005

Nedić J, Vassilicos JC, Ganapathisubramani B (2013) Axisymmetric turbulent wakes with new nonequilibrium similarity scalings. Phys Rev Lett 111:144503

Nidhan S, Chongsiripinyo K, Schmidt OT, Sarkar S (2020) Spectral proper orthogonal decomposition analysis of the turbulent wake of a disk at Re = 50 000. Phys Ref Fluids 5:124606

Obligado M, Dairay T, Vassilicos JC (2016) Non-equilibrium scalings of turbulent wakes. Phys Rev Fluids 1:044409

Pal A, Sarkar S, Posa A, Balaras E (2017) Direct numerical simulation of stratified flow past a sphere at a subcritical Reynolds number of 3700 and moderate Froude number. J Fluid Mech 826:5–31

Raffel M, Willert C, Scarano F, Kahler C, Wereley S, Kompenhans J (2018) Particle image velocimetry: a practical guide. Springer, New York

Saunders DC, Frederick G, Drivas TD, Wunsch S (2020) Self-similar decay of the drag wake of a dimpled sphere. Phys Rev Fluids 5:124607

Swain LM (1929) On the turbulent wake behind a body of revolution. Proc R Soc Lond 125:647–659

Tennekes H, Lumley JL (1972) A first course in turbulence. MIT, Cambridge, MA

UVMAT Particle Image velocimetry program (2018) http://servforge.legi.grenoble-inp.fr/projects/soft-uvmat